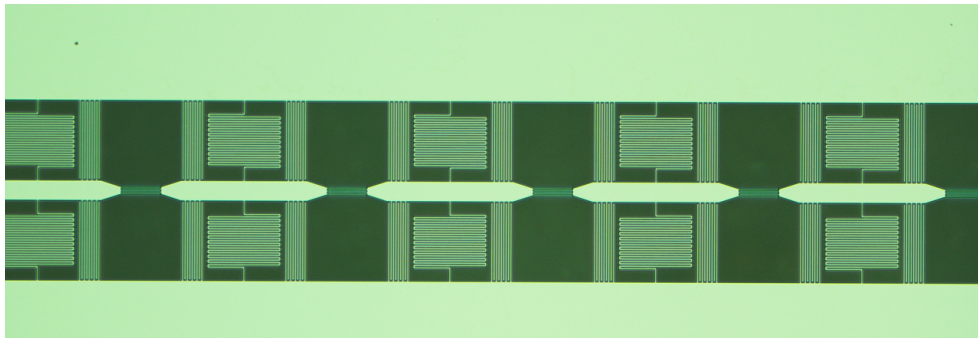


### Microwave Waveguides with Engineered Dispersion based on Arrays of Lumped-Element Resonators

Simon Mathis<sup>1</sup>

supervised by  
Jean-Claude BESSE and Simone GASPARINETTI

October 19, 2017



#### Abstract

We designed and measured a slow light waveguide in the microwave domain based on an architecture of periodic arrays of lumped element resonators. The experiment confirmed that many physical properties of such resonator arrays can be understood based on the simple model of a coupled LC resonator chain. With the measured chip set a group delay of 17 ns was achieved in a transmission band of 10 MHz width in a ten site resonator array. This delay is two orders of magnitude larger than the delay obtained by a transmission line of the same length as the resonator array. In this report we examine the physical properties of coupled resonator arrays based on lumped element resonators and provide insights for improving the design of such arrays.

---

<sup>1</sup>mathissi@student.ethz.ch

# Contents

<b>1</b>	<b>Introduction</b>	<b>2</b>
<b>2</b>	<b>Theoretical Background</b>	<b>3</b>
2.1	Resonators . . . . .	3
2.1.1	Lumped Element Resonators . . . . .	3
2.1.2	Coplanar Waveguide Resonators . . . . .	5
2.2	Coupled Resonator Arrays . . . . .	5
2.2.1	Hamiltonian Formalism . . . . .	5
2.3	Transfer Matrix Method . . . . .	7
2.3.1	Dispersion Relation from Transfer Matrices . . . . .	7
2.3.2	Scattering Matrix . . . . .	8
2.4	Finite Coupled Resonator Arrays . . . . .	9
2.4.1	Simulation of Finite Coupled Resonator Arrays . . . . .	9
2.4.2	Matching Condition for Coupling to the Outside . . . . .	10
2.4.3	Transmission Amplitude Profile . . . . .	12
2.4.4	Characterization of Pulse Transfer through a CRA . . . . .	13
<b>3</b>	<b>Physical Design of Lumped Element CRAs</b>	<b>15</b>
3.1	General Design . . . . .	15
3.2	Inductors . . . . .	17
3.3	Capacitors . . . . .	18
3.4	Summary . . . . .	18
<b>4</b>	<b>Experimental Studies</b>	<b>19</b>
4.1	Experimental Setup and Conditions . . . . .	19
4.2	Experimental Results . . . . .	19
4.2.1	Symmetric vs. Non-Symmetric Unit Cell . . . . .	19
4.2.2	Scaling of the Transmission Envelope and Delay . . . . .	21
4.2.3	Fabrication Inhomogeneities . . . . .	23
4.2.4	TL-Turns vs. R-Turns . . . . .	23
4.2.5	Parameter Extraction . . . . .	25
<b>5</b>	<b>Conclusion and Outlook</b>	<b>29</b>
<b>A</b>	<b>Motivation of the Bloch Condition</b>	<b>33</b>
<b>B</b>	<b>Transformation: Design and Resonator Parameters</b>	<b>33</b>
<b>C</b>	<b>Definition of the group delay</b>	<b>33</b>
<b>D</b>	<b>Inductance contribution from the island</b>	<b>34</b>
<b>E</b>	<b>Parameter Estimation charts</b>	<b>34</b>

# 1 Introduction

The initial goal of this project was to obtain slow light in the microwave domain. A slow light waveguide is an essential tool to create, together with a superconducting switch [1], non-reciprocity in quantum circuit electrodynamic experiments, or to study long distance interactions between qubits. Slow-light waveguides can also give rise to atom-field dressed states with the potential to experimentally investigate atom-photon bound states [2].

Our realization of a slow light device is based on the idea that the dispersion relation in periodic structures flattens out around the transmission band edges. The group velocity is given by the derivative  $\partial\omega/\partial k$  of the dispersion relation and is therefore small in regions where the dispersion relation is flat. This implies that for frequencies close to the band edge one can obtain a slow group velocity in combination with a large transmission bandwidth [Section 2.2]. As a result of this implementation our slow light waveguides work at frequencies in direct vicinity of a photonic bandgap, which allows to investigate microwave photonics around the band edge. One could use our structures for example to study photon-mediated interactions between atoms with frequencies in the band gap.

In our physical implementation the required periodicity is provided by arrays of coupled lumped element resonators. By tuning the design parameters of these arrays we can engineer the dispersion relation to obtain a specific target frequency, transmission bandwidth and group velocity. To guide the design of our structures and the tuning of the relevant parameters we defined a slow light waveguide by the following two essential features. Firstly it must transmit a pulse at the target frequency with a spectral width of 10 MHz or more without significant attenuation. The limit of 10 MHz was chosen because it corresponds to photons emitted as fast as 15 ns, which is less than typical values in waveguides. Secondly, it should slow down this pulse by at least two orders of magnitude as compared to propagation in a typical transmission line. During the project we designed the slow light waveguides with the additional feature that the photon mode used to generate slow light is approximately equally spread over all sites. This third condition is important to enable coupling qubits to various sites of the structure, an application for which we envision our structures can be used.

We will review the fundamental theory required to interpret the experimental results of this project in Section 2. Section 3 briefly summarizes the experimental setup and sets the stage for the subsequent analysis. We present our experimental results in Section 4 and finally summarize the main outcomes of this project in Section 5. An outlook for future improvements and applications of our structures is also given in this section.

## 2 Theoretical Background

### 2.1 Resonators

Superconducting resonators are a fundamental building block of circuit quantum electrodynamics. They are categorized into linear resonators, which are used for example to dispersively read-out the state of a qubit, and nonlinear resonators, which are essential to building qubits. In our discussion of coupled resonator arrays we will work exclusively with linear resonators since they are easier to control and modify.

If we are only interested in the lowest mode, a linear resonator can be described by its resonance frequency  $\omega_0 = 2\pi f_0$  and the total rate at which energy stored in the resonator is lost. The quality factor of a resonator offers a convenient description of this energy loss and is defined by

$$Q := \omega_0 \frac{\text{Energy stored}}{\text{Power loss}} \approx \frac{f_0}{\Delta f_0}. \quad (1)$$

Here  $f_0$  is the resonance frequency and  $\Delta f_0$  the full width at half max (FWHM) of the resonance. It is useful to make a distinction between losses inherent to the structure, so called internal losses, and losses due to a coupling of the environment termed external losses. The internal loss rate is commonly called  $\gamma$  and for microwave resonators it describes resistive, radiative and dielectric losses to the environment. The external loss rate  $\kappa$  accounts for losses due to coupling to other circuit elements. Likewise the quality factor is split into an internal part  $Q_{int}$  and an external part  $Q_{ext}$ .

#### 2.1.1 Lumped Element Resonators

When a certain circuit element is much smaller than the wavelength of light considered, we can model it as a point-like object characterized by a complex impedance  $Z$ . This approximated element is then known as lumped element and can be described by conventional circuit theory. By combining individual lumped elements, one can build a lumped element resonator. In the following we will concentrate on parallel RLC resonators displayed in Fig. 1.

**RLC Resonators** For an unloaded RLC, as shown in Fig. 1(a), we find

$$\omega_0 = \frac{1}{\sqrt{LC}} \quad (2)$$

$$Z = \sqrt{\frac{L}{C}} \quad (3)$$

$$\gamma = \frac{1}{RC} = \frac{\omega_0}{Q_{int}}. \quad (4)$$

The limiting case where  $R = 0$  is known simply as LC resonator. In this case the internal Q-factor  $Q_{int}$  is infinite signifying that no energy is dissipated.

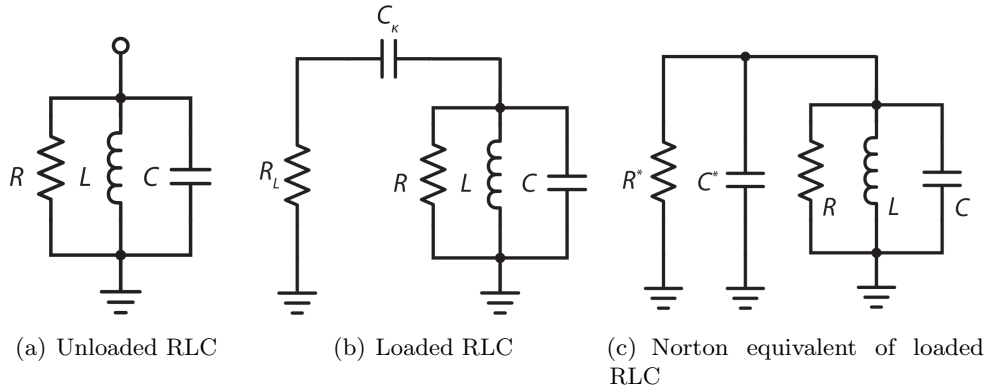


Figure 1: RLC Schematics. (a) Unloaded parallel RLC circuit. (b) Parallel RLC circuit with a capacitive coupling  $C_\kappa$  to the load  $R_L$ . (c) Norton equivalent of the capacitively coupled RLC oscillator. Symbols are explained in the text.

When the RLC resonator is coupled to an external circuit it is called loaded. In this case the above relations are renormalized. To understand the renormalization for a capacitively coupled resonator (Fig. 1(b)) it is instructive to use Norton's Theorem and transform this circuit to its Norton equivalent. This Norton equivalent is displayed in Fig. 1(c). Notice that it is again an RLC resonator with total resistance  $R_\Sigma = (1/R + 1/R^*)^{-1}$  and total capacitance  $C_\Sigma = C + C^*$ . The equivalent parameters for this circuit around resonance are [3]

$$C^* = \frac{C_\kappa}{1 + (\omega_0 C_\kappa R_L)^2} \approx C_\kappa \quad (5)$$

$$R^* = \frac{1 + (\omega_0 C_\kappa R_L)^2}{\omega_0^2 C_\kappa^2 R_L} \approx \frac{1}{C_\kappa^2 R_L \omega_0^2}, \quad (6)$$

such that the renormalized resonance frequency becomes  $\omega_r = 1/\sqrt{LC_\Sigma}$ . For microwave circuits one typically uses  $R_L = Z_0 = 50 \Omega$ , since this is the characteristic impedance of the waveguides used to couple to the resonator.

In the equivalent circuit  $R^*$  describes losses due to coupling of the resonator to the rest of the circuit and  $R$  describes losses to the environment. The coupling rate of the resonator to the circuit is  $\kappa = 1/(R^* C_\Sigma)$  and the internal loss rate is  $\gamma = 1/(RC_\Sigma)$ . This results in a loaded Q-factor of

$$\frac{1}{Q_L} = \frac{1}{Q_{int}} + \frac{1}{Q_{ext}} = \frac{\gamma}{\omega_r} + \frac{\kappa}{\omega_r}. \quad (7)$$

From this equation it can be seen that resonators with  $Q_{ext} \ll Q_{int}$  or equivalently  $\kappa \gg \gamma$  may in practice be modeled by LC resonators. This will be the case for all structures discussed in this report by design.

### 2.1.2 Coplanar Waveguide Resonators

Another type of resonators that are used in circuit quantum electrodynamics are coplanar waveguide resonators. These CPW resonators have a specific length that allows only a discrete set of modes to propagate through without significant attenuation.

Even though CPW resonators are distributed circuit elements, they can be approximated by an RLC resonator around resonance [4]. The RLC equivalent parameters for the  $n$ -th resonance are

$$L_n = \frac{2}{n^2\pi^2}L_l l \quad (8)$$

$$C = \frac{1}{2}C_l l \quad (9)$$

$$R = \frac{Z_0}{\alpha l}, \quad (10)$$

where  $L_l$  ( $C_l$ ) is the inductance (capacitance) per unit length,  $\alpha$  the attenuation constant of the waveguide,  $Z_0 = \sqrt{L_l/C_l}$  the waveguide impedance and  $l$  the length of the coplanar waveguide. Note in particular that the first resonant mode of a CPW resonator with impedance  $Z_0$  corresponds to an RLC resonator with the same resonance frequency but impedance  $(2/\pi)Z_0$ . This means that one has to take an additional factor  $2/\pi$  into account when trying to match the impedance of an RLC resonator with that of a coplanar waveguide resonator at the same frequency.

## 2.2 Coupled Resonator Arrays

### 2.2.1 Hamiltonian Formalism

A schematic representation of a coupled resonator array (CRA) is shown in Fig. 2(a). Assuming periodic boundary conditions and only nearest-neighbor coupling, a coupled resonator array with  $N$  sites can be described by the tight binding Hamiltonian

$$H = \hbar\omega_0 \sum_j^N a_j^\dagger a_j - \hbar J \sum_j^N (a_j^\dagger a_{j-1} + a_{j-1}^\dagger a_j), \quad (11)$$

where  $a_j$  ( $a_j^\dagger$ ) are the bosonic annihilation (creation) operators for the  $j$ -th resonator located at  $z_j$ ,  $\omega_0$  is the resonance frequency of an individual resonator and  $J$  is the nearest-neighbor coupling. This Hamiltonian has the form of a standard tight-binding Hamiltonian. For capacitively coupled resonators the nearest neighbor coupling is given by

$$J = \frac{1}{2} \frac{C_\kappa}{C_\Sigma} \omega_0. \quad (12)$$

The transform of this Hamiltonian into a normal mode representation is achieved with the momentum operators  $a_k = \frac{1}{\sqrt{N}} \sum_j e^{ikz_j} a_j$ , where  $k \in (-\pi, \pi]$  is the photon wavevector.

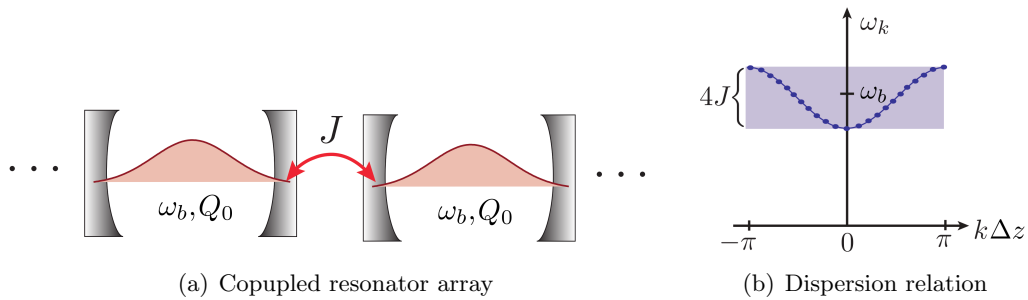


Figure 2: (a) Schematic of a coupled resonator array. Individual sites have the bare resonance frequency  $\omega_0$  and a quality factor  $Q_0$ . The inter-site coupling is given by  $J$ . (b) Dispersion relation for a coupled resonator array without edge effects, i.e. under the assumption of periodic boundary conditions. Note that for  $N$  sites there are  $N$  allowed modes that can propagate in the CRA, indicated by blue dots on the dispersion relation. As  $N \rightarrow \infty$  the modes start to form a continuum (transmission band) in the blue shaded region. Figure adapted from [2].

In this representation the Hamiltonian takes a diagonal form  $H = \sum_k \hbar \omega_k a_k^\dagger a_k$  with the photon frequencies

$$\omega_k = \omega_0 - 2J \cos(k\Delta z), \quad (13)$$

where  $\Delta z = z_{j+1} - z_j$  is the lattice constant [2]. Eq. (13) is known as dispersion relation.

**Infinite Site Limit** For a coupled resonator array of  $N$  sites, there are  $N$  allowed modes that can propagate through the array. As  $N \rightarrow \infty$  the mode spacing goes to zero and  $k$  becomes a continuous variable. In this limit the  $\omega_k$  form a continuous band of width  $4J$  centered around  $\omega_0$ , as plotted in Fig. 2(b). In the infinite site limit frequencies within this band can propagate through a lossless CRA with unit transmission, whereas frequencies outside the band are not transmitted at all. Thus we subsequently refer to this band as transmission band.

The group velocity for wave packets in the infinite CRA is readily obtained to be

$$v_g(\omega) = \left. \frac{\partial \omega_k}{\partial k} \right|_{\omega_k = \omega} = \Delta z \sqrt{4J^2 - (\omega - \omega_0)^2}, \quad (14)$$

which vanishes at the band edge, i.e. for  $\omega = \omega_0 \pm 2J$ , and is maximal in the center of the band. This makes CRAs excellent tools for dispersive engineering. By choosing the operating frequency close to the band gap the light can in principle be made arbitrarily slow, resulting in a high group delay.

**Finite Site Treatment** It is also possible to treat a finite number of sites in this Hamiltonian formalism. To do so the Hamiltonian  $H_N$  in Eq. (11) can be cast into an



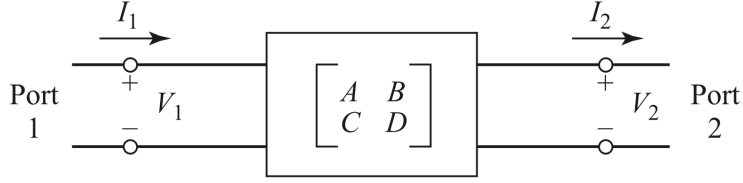


Figure 3: Illustration of the transfer matrix method. The ABCD matrix relates the voltage and current at one port (or point in the circuit) to the voltage and current at another port. Figure adapted from [3].

Bloch condition<sup>3</sup>

$$V(z + \Delta z) = V(z)e^{ik\Delta z} \quad (20)$$

$$I(z + \Delta z) = I(z)e^{ik\Delta z} \quad (21)$$

on the allowed modes of the system [5]. Here  $\Delta z$  is the length of a single unit cell. Using the transfer matrix formalism, we find the equation

$$\begin{pmatrix} V(z + \Delta z) \\ I(z + \Delta z) \end{pmatrix} = e^{ik\Delta z} \begin{pmatrix} V(z) \\ I(z) \end{pmatrix} = \mathbf{M}_{cell}(\omega) \begin{pmatrix} V(z) \\ I(z) \end{pmatrix}, \quad (22)$$

which relates the voltage and current between neighboring sites. A solution to this eigenvalue problem exists only under the condition that  $\det(\mathbf{M}_{cell}(\omega) - \mathbf{1}e^{ik\Delta z}) = 0$ , which yields the dispersion relation for an infinitely long cavity array

$$\cos(k\Delta z) = \text{Tr}(\mathbf{M}_{cell})/2. \quad (23)$$

The dispersion relation for the unit cell in Fig. 5 is shown in Fig. 4. The shaded region corresponds to the band of allowed frequencies that can propagate through the coupled resonator array.

### 2.3.2 Scattering Matrix

The connection between the transfer formalism and physically accessible properties in the laboratory is given by the scattering matrix. To formulate the scattering matrix for a specific frequency one considers each port of the circuit element connected to an infinite waveguide in which incoming/outgoing plane waves propagate. The scattering matrix is then defined via the scattering of these plane waves as

$$\begin{pmatrix} V_1^- \\ V_2^- \end{pmatrix} = \mathbf{S} \begin{pmatrix} V_1^+ \\ V_2^+ \end{pmatrix} = \begin{pmatrix} S_{11} & S_{12} \\ S_{21} & S_{22} \end{pmatrix} \begin{pmatrix} V_1^+ \\ V_2^+ \end{pmatrix}. \quad (24)$$

In this context  $V_i^+$  ( $V_i^-$ ) is the voltage of the wave going into (coming out of) port  $i$ . By setting  $V_2^+ = 0$  in Eq. 24 it can be seen that the matrix element  $S_{11}$  is the reflection

<sup>3</sup>For a discussion on the physical intuition we refer to the Appendix.

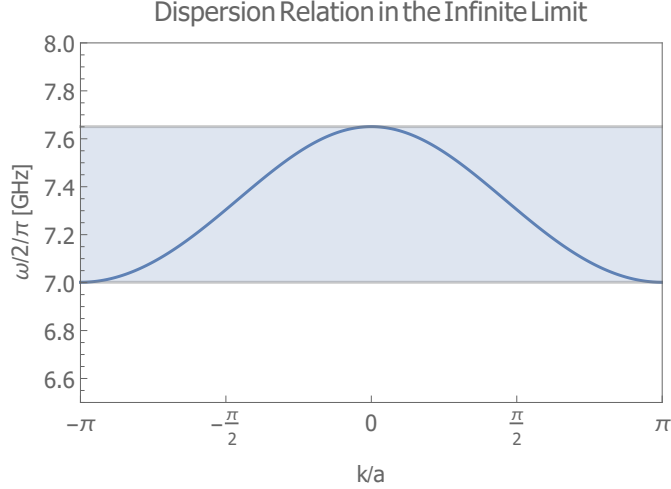


Figure 4: The dispersion relation for the unit cell shown in Fig. 5. The parameters were chosen to be  $L = 0.75$  nH,  $C = 577$  fF,  $C_t = 2C_\kappa = 56$  fF. This yields a band gap frequency of  $f_g = 7$  GHz and a coupling of  $J/2\pi = -162$  MHz. Note that the width of the band is  $4J$  as obtained in the Hamiltonian formalism.

coefficient from port 1 to port 1 and that  $S_{21}$  is the transmission coefficient from port 1 to port 2. These reflection and transmission coefficients can be measured experimentally with the help of a network analyzer.

The scattering matrix can be connected to the transfer matrix via the Ohm's law  $Z(x) = V(x)/I(x)$ , where  $Z$ ,  $V$  and  $I$  are the complex impedance, voltage and current at point  $x$  respectively. The transformations are given by [3]

$$\mathbf{S} = \frac{1}{A + \frac{B}{Z_0} + CZ_0 + D} \begin{pmatrix} A + \frac{B}{Z_0} - CZ_0 - D & 2(AD - BC) \\ 2 & -A + \frac{B}{Z_0} - CZ_0 + D \end{pmatrix}, \quad (25)$$

with the port impedance  $Z_0$  taken to be the same for ports 1 and 2 in this formula.

## 2.4 Finite Coupled Resonator Arrays

In this section we discuss how to simulate finite coupled cavity arrays with the matrix methods introduced above and use these simulations to study their properties.

### 2.4.1 Simulation of Finite Coupled Resonator Arrays

The simplest theoretical model of a finite coupled resonator array is a chain of identical LC resonators with nearest neighbor coupling only. Such a model has five relevant parameters:

- the resonator inductance  $L$ ,

- the resonator capacitance  $C$ ,
- the inter-site coupling capacitance  $C_\kappa$ ,
- the termination capacitance  $C_t$ ,
- the number of sites  $N$ .

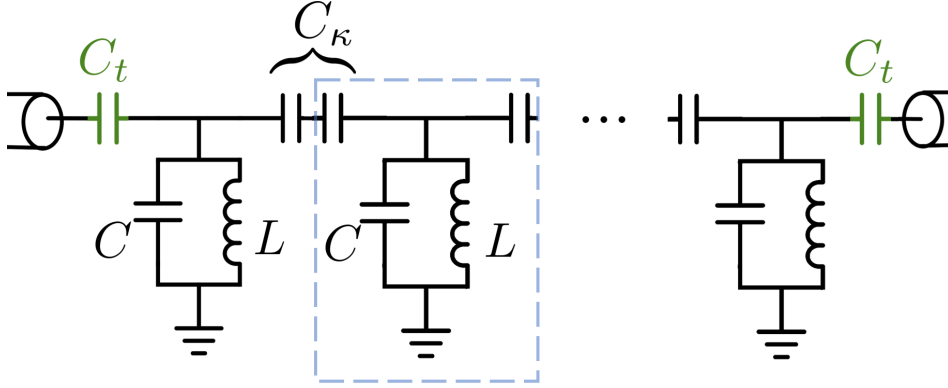


Figure 5: A coupled resonator array built by a chain of capacitively coupled identical LC resonators. The unit cell with transfer matrix  $\mathbf{M}_{\text{cell}}$  is indicated by the blue box. It is understood that the black dots represent a repetition of this unit cell. In this model only the first and last cell may differ from the unit cell in their coupling  $C_t$  to the outside to achieve impedance matching with the outside.

Using the matrix formalism above, the total transfer matrix for an LC resonator chain with  $N$  sites is

$$\mathbf{M}_{\text{tot}} = \mathbf{M}_1 (\mathbf{M}_{\text{cell}})^{N-2} \mathbf{M}_2. \quad (26)$$

In this equation  $\mathbf{M}_{\text{cell}}$  is the transfer matrix of the unit cell in the blue box in Fig. 5 and  $\mathbf{M}_1$  ( $\mathbf{M}_2$ ) refer to the edge cells where the left (right) capacitor is replaced by  $C_t$  as compared to the unit cell. The scattering parameters, which can be compared to experiments, then follow directly from the transform of the total transfer matrix to the scattering matrix via Eq. (25).

While the LC parameters ( $C, L, C_\kappa, C_t, N$ ) are useful for designing a coupled resonator array, they are not optimal for analyzing the underlying physics. This is because the physical effects that take place depend on a combination of these five parameters. For a transparent analysis of the physical properties of a CRA the parameters ( $\omega_0, Z, J, \delta, N$ ) are more useful. These parameters were defined in Sections 2.1.1 and 2.2.1 and are summarized again in Appendix B.

#### 2.4.2 Matching Condition for Coupling to the Outside

For linear CRAs with a finite number of sites edge effects become important. The question of how to choose the termination capacitance  $C_t$  depends on the experimental

question that we want to investigate. Since we plan to couple qubits to different sites in the CRA, this raises the question of how to terminate the array in such a way that: (i) the frequency of the targeted mode does not depend on the site number  $N$ , and (ii) the targeted mode is fully delocalized, that is, it equally occupies all sites. This question can be investigated in the Hamiltonian formalism introduced in Section 2.2.1 by finding the eigenvalues and eigenvectors of the Hamiltonian  $H_N$ .

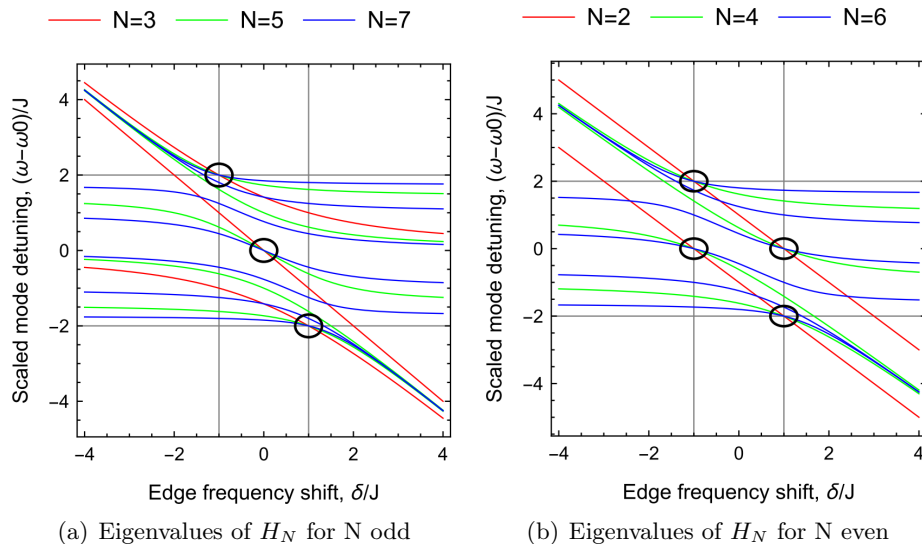


Figure 6: The eigenvalues of the Hamiltonians  $H_N$  [Section 2.2.1] are shown for different values of  $N$  as a function of the edge frequency renormalization  $\delta$ . Panel (a) shows the eigenvalues of  $H_N$  for even  $N$  and panel (b) shows the eigenvalues for odd  $N$ . All eigenvalues fall in the band  $\omega_0 \pm 2J$  when  $|\delta| \leq J$ , which is marked by the two horizontal black lines in the figure. Fixed points, i.e. eigenvalues that do not depend on  $N$  for given values of  $\delta$ , are encircled. Further explanation is given in the text. These plots are courtesy of Simone Gasparinetti.

It turns out [Fig. 6] that there are three matching conditions for  $C_t$  that fulfill requirements (i) and (ii) from above ( $\delta = J_t - J$ ):

1.  $C_t = 0$ , that is  $\delta = -J$ . This matching condition corresponds to leaving the edge sites open or coupling them to the outside with capacitance  $C_t \ll C_\kappa$ . For all  $N$  there is a delocalized mode at the top of the band ( $\omega_0 + 2J$ ). For even  $N$  there is also one at the center of the band ( $\omega_0$ ).
2.  $C_t = C_\kappa$ , that is  $\delta = 0$ . This means choosing the external coupling to be the same as the inter-site coupling. For odd  $N$  there is a delocalized mode at the center of the band, but only odd sites are occupied by this mode.
3.  $C_t = 2C_\kappa$ , that is  $\delta = J$ . For all  $N$  there is a delocalized mode at the bottom of the band ( $\omega_0 - 2J$ ). For even  $N$  there is an additional one at the center of the

band. This condition is most promising for experiments, since the mode at the lower edge of the band can be coupled to the environment at a rate comparable to  $J$ . We assume this matching condition for the remainder of this report.

Notice that this matching condition for fulfilling requirements (i) and (ii) does not depend on the external load  $Z_0$ . The impedance  $Z_0$  does however affect the coupling rate to the environment.

### 2.4.3 Transmission Amplitude Profile

In the infinite site limit  $N \rightarrow \infty$  the transmission amplitude  $S_{12}$  develops a flat band around the resonance frequency of a unit cell (see Sec. 2.2.1). Instead, for finite CRAs the region of the developing transmission band features  $N$  resonances whose widths depend on the number of sites, the individual resonator impedances, the inter-site coupling and most importantly the coupling to the outside. A specific example is shown in Fig. 7 for illustration.

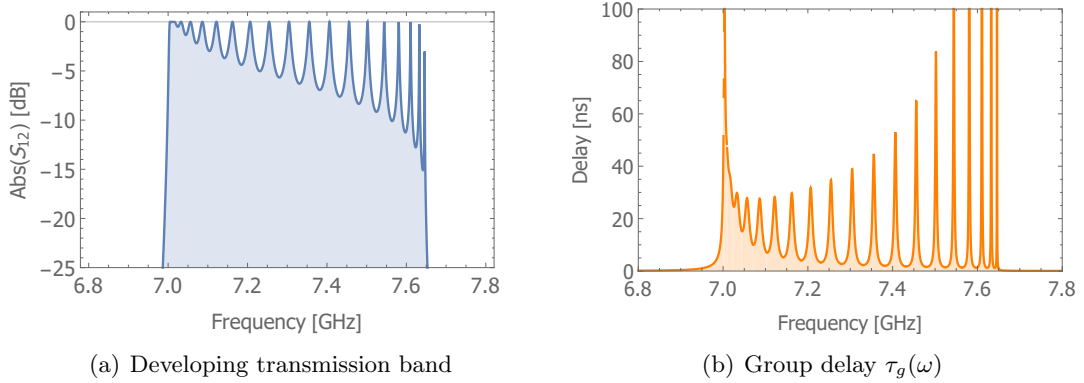


Figure 7: (a) The transmission amplitude  $|S_{12}|$  is plotted for a finite CRA formed by 20 lossless LC resonators. (b) The corresponding group delay for the same CRA. The calculation is explained in the text. The plot parameters correspond to the schematic in Fig. 5 and are  $L = 0.75$  nH,  $C = 577$  fF,  $C_t = 2C_\kappa = 56$  fF with  $N = 20$  sites. This corresponds to the resonator parameters  $\omega_0/2\pi = 7.304$  GHz,  $Z = 34.4 \Omega$ ,  $J/2\pi = 162$  MHz and  $\delta = J$ .

As is the case of an infinite array, the spectrum of  $S_{12}$  for a finite CRA starts to form sharp band gaps around  $\omega_0 \pm 2J$ . In between this interval there are  $N$  resonant modes, i.e. the number of modes or resonances in  $S_{12}$  equals the number of sites. Nevertheless, the envelope of  $S_{12}$  is independent of the number of sites  $N$  for  $N > 2$ .

A larger inter-site coupling  $J$  leads to broadening of the resonances in the transmission spectrum. This leads to increased hybridization of peaks. For the matching  $C_t = 2C_\kappa$  the spectrum of  $S_{12}$  develops a small transmission band around  $\omega_0 - 2J$  due to the hybridization of several peaks. The extent of this small band depends on  $J$  and is typically on the order of tens of MHz in our range of parameters.

#### 2.4.4 Characterization of Pulse Transfer through a CRA

A measure for the temporal delay of a narrow pulse in frequency space due to propagation through a circuit element is given by the group delay<sup>4</sup>. It can be calculated as

$$\tau_g(\omega) = - \left. \frac{\partial \text{Arg}(S_{12})}{\partial \omega} \right|_{\omega} \quad (27)$$

and for illustration the group delay of a finite CRA is plotted in Fig. 7(b).

In our simulations we found that the delay at the bottom edge scales linearly with the number of cells  $N$ . More generally we found an approximately linear scaling of the delay with  $N/J$ , which is consistent with the intuition that for the fully delocalized edge mode the transport takes place via site-to-site hopping at a rate  $J$ .

For the example in Fig. 7 a delay on the order of 40 ns can be achieved with approximately unit transmission within the small transmission band at  $\omega_0 - 2J$ . To set this into context, consider that the length of a 20 site array in the geometry presented in Section 3 is roughly 11 mm. A transmission line of the same length would give a delay of about 0.1 ns, which is more than two orders of magnitude smaller than the delay obtained from the chain of LC resonators.

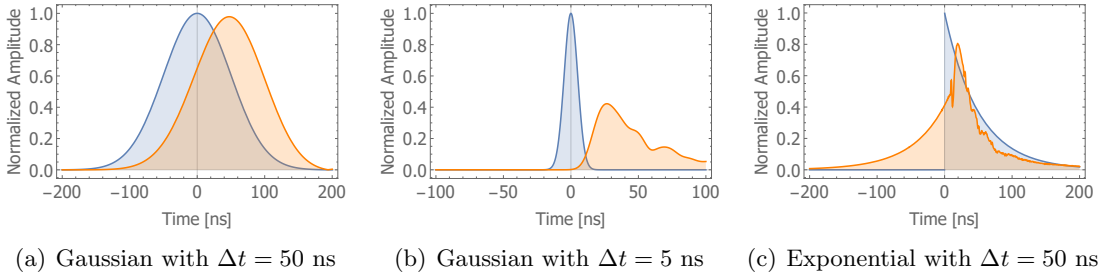


Figure 8: Wave packet distortion for different temporal pulse envelopes after propagation with a carrier frequency  $\omega_c = 7.01$  GHz through the CRA in Fig. 7. The input (output) pulse is shown in blue (orange). (a) Distortion of a Gaussian wave packet  $f_{in} = e^{-t^2/(2\Delta t^2)}$  with  $\Delta t = 50$  ns. (b) Distortion of a Gaussian wave packet with  $\Delta t = 5$  ns. (c) Distortion of an exponential packet  $f_{in} = e^{-t/\Delta t}\theta(t)$  with  $\Delta t = 50$  ns. The plot parameters are as in Fig. 7.

The group delay can be used to characterize the propagation of pulses with a frequency spectrum narrow enough that they extend only over one individual peak in the structure of  $S_{12}$ . For pulses with frequency components extending over several peaks significant distortion of the pulse shape may occur. To capture the distortion of the wave packet a complete Fourier treatment is necessary. In such a treatment the temporal envelope of a pulse is first transformed to Fourier space, then multiplied with the complex transmission amplitude  $S_{12}(\omega)$  and finally converted back to the time domain by taking an inverse Fourier transform<sup>5</sup>. As an example, the distortion of two Gaussian and one half-sided

<sup>4</sup>For a definition and a proof of its connection to the delay of a pulse consult Appendix C.

<sup>5</sup>See Eq. (35) in Appendix C.

exponential wave packet after propagation through the CRA in Fig. 7 is shown in Fig. 8. Note that the distortion of the exponential pulse is more pronounced than that of a Gaussian with comparable width since its extent in frequency space is larger.

### 3 Physical Design of Lumped Element CRAs

We now turn to the physical realization of a lumped element coupled resonator array. In this section we present the main characteristics of the design that we employed in the following experimental study. Also, the parameter estimates as obtained from electromagnetic simulations are discussed.

#### 3.1 General Design

The physical implementation of our CRA is based on the LC chain circuit discussed in Sec. 2. For a first impression of the overall design a microscope image of one segment of the CRA is displayed in Fig. 9. We highlighted where the main contributions to the capacitances  $C$ ,  $C_\kappa$  and the inductance  $L$  come from in one unit cell. The coupling to the outside ( $C_t$ ) is also achieved with a finger capacitor, which differs from  $C_\kappa$  only in its larger number of fingers. All structures are etched using Reactive Ion Etching (RIE) from a thin-film of superconducting niobium (150 nm thick) on top of a sapphire substrate (0.43 mm thick), after resist patterning in a lithography step.

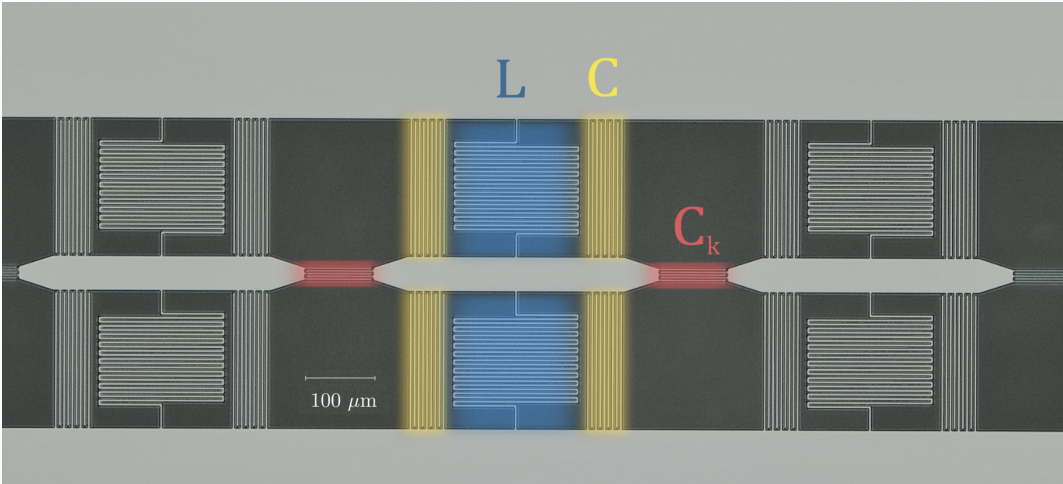


Figure 9: A false-color micrograph of a CRA segment. The capacitor  $C$  and the inductor  $L$  for a single cell are shaded yellow and blue respectively. The two coupling capacitors  $C_\kappa$  to adjacent sites are colored in red. The superconducting niobium thin film is light in this picture and the sapphire substrate appears dark.

In the present design (Qudev Mask M77) each unit cell has two symmetry axes, providing left-right and top-bottom symmetry. We chose this highly symmetric design because it reduces parasitic effects from compensation currents that have to flow around the structure. As can be seen in the microscopic image, a single resonator with one coupler extends for slightly more than 0.5 mm. To set the lengths into context we note that the on-chip wavelength is approximately 18.6 mm at 7 GHz, leading to a phase roll

of about 20 deg per mm of transmission line. As a self-consistency check for the lumped element approximation, we also should verify that our resonators fulfill the condition  $d_{\text{cell}} \ll \lambda$ . In our case this relation holds well as the cell size is a factor 30 smaller than the relevant wavelength<sup>6</sup>.

From geometric considerations we see that a typical 7x4 mm chip can accommodate 10 sites in one line. This raises one of the main challenges of implementing long on-chip CRAs, that is how to turn at the end of a linear array segment. Since the creation of the flat transmission band with a sharp band gap at around  $\omega_0 - 2J$  requires a perfectly periodic structure, it is essential to design the turns in such a way that resonators at the end of a line look effectively identical to resonators in the linear segment. We examined two options for creating these turns, a resonator turn (R-turn) and a transmission line turn (TL-turn).

**R-Turn** The R-turn CRAs are designed with the coupling capacitors  $C_\kappa$  at the end of a linear segment at an angle of 45 degrees, such that they can couple to a resonator which is tilted 90 degrees with respect to the linear array. This rotated resonator at the ‘edge’ of the linear segment can then couple to the next linear array segment with another coupling capacitor at 45 degrees. This allows one to build up a meandering array of lumped element resonators. The challenge of this geometry is to ensure that the edge environment matches as closely as possible the environment seen by a resonator in the linear segment. Moreover, it is essential that the properties of the rotated resonator are equal to the properties of the resonators in the linear array.

**TL-Turn** The TL-turns on the other hand simply couple two linear arrays by a piece of transmission line. Here too the matching condition for the end couplers, as well as the length and impedance of the transmission line are important. There are two options for choosing the length.

1.  $l \ll \lambda$ , such that the phase difference acquired by propagation through the waveguide is close to zero and resonances in the waveguide are at very high frequencies (several tens of GHz). In simulations we found that the optimal matching condition for the couplers at edge sites is then given by choosing them to be equal to  $C_t$ . This makes intuitive sense since in the limit where the transmission line is short we have a series circuit of the two edge couplers. This halves their capacitance and thereby makes the coupling equal to the standard inter-site coupling capacitance  $C_\kappa$ .
2.  $l = \lambda/2$ , that is the transmission line is used as a CPW resonator at the same frequency as the LC unit cells. To have the CPW resonator effectively mimic a unit cell its properties must be matched to the LC resonators with the conditions in Section 2.1.2. In this case the optimal edge termination is achieved if the edge couplers have the inter-site capacitance  $C_\kappa$ .

---

<sup>6</sup>For a more rigorous validity test of the lumped element approximation one needs to simulate the behavior of parasitic effects in a high-frequency electromagnetic simulation. Such a procedure was carried out for a similar resonator geometry in Ref. [6], affirming the lumped nature of our resonators.

### 3.2 Inductors

To create inductances we used meandering line inductors. These are two dimensional structures where the (super-) conducting line is meandered back and forth to maximize the total length and hence inductance<sup>7</sup>. The design parameters for the chip series analyzed in this report (Qudev M77) along with estimates for our inductors are summarized in Tab. 1. These estimates have to be taken with care, since there are several effects that can lead to spurious inductive contributions in our structures. We discuss the most important of these in the subsequent paragraphs. For better inductance estimates a full electromagnetic simulation is necessary.

Meander Inductor ( $L$ )	
No. of turns	21
Turn length ( $h$ )	180 $\mu\text{m}$
Line width ( $w$ )	3 $\mu\text{m}$
Gap width ( $d$ )	3 $\mu\text{m}$
Expected geom. inductance	1.5 (2) nH

Table 1: Design details of the meandering inductors on the M77 chip series. The geometric inductance estimates are calculated with the methods presented in [7] (see also [6]). From the discussion in [7] we expect this estimate to be accurate within 10%. Note that the inductors in our design are in parallel, hence the total inductance of one site is half of the inductance for a single inductor  $L \approx 0.74(9)$  nH.

**Spurious currents and island contributions** We remark that the quoted theoretical inductance estimate for an equivalent inductor turned out to consistently be about 0.2 nH lower than experimentally obtained values in Ref. [6]. In their case they concluded that this effect arises because the island of the resonator contributes to the total inductance. A calculation of the expected series inductance from the island [Appendix D] indicates that this effect is on the order of 0.15 nH for the island geometry in Ref. [6]. Since the design in Ref. [6] has none of the symmetry axes present in our design, we suspect that some of the discrepancy in inductance in their case might also come from compensation currents around the structure.

**Kinetic inductance** The contribution from kinetic inductance for a design similar to ours was measured to be of the order of 0.06 nH at 4.2 K [6], which is about 4 % of the estimated geometric inductance value. This contribution becomes irrelevant at the lower temperatures at which superconducting qubits are typically operated (<100 mK). We refer to Ref. [6]

<sup>7</sup>For a more detailed treatment we refer the reader to [6] and literature therein.

### 3.3 Capacitors

In the present design we exclusively used interdigital finger capacitors, due to their compact geometry and the approximately linear scaling of the capacitance with the number of fingers (compare Appendix E). The design parameters for the finger capacitors are summarized in Table 2. To find the expected capacitances, we have simulated the different geometries with the finite- element electromagnetic field simulation software ANSYS Maxwell.

	$C$	$C_\kappa$	$C_t$
Finger no.	36 (4 x 9)	5	9 / 10 / 11
Finger length	197 $\mu\text{m}$	98 $\mu\text{m}$	98 $\mu\text{m}$
Finger width	3 $\mu\text{m}$	2 $\mu\text{m}$	2 $\mu\text{m}$
Finger gap	3 $\mu\text{m}$	2 $\mu\text{m}$	2 $\mu\text{m}$
Simulated cap.	430 fF	28.5 fF	- / 54.5 fF / -
Expected cap.	400(30) fF	24(2) fF	49(5) fF / 54(5) fF / 59(5) fF

Table 2: Design details of the interdigital capacitors used for the M77 chip series. The simulated capacitances were obtained from DC simulations with ANSYS Maxwell. The expected capacitances for our design from an extrapolation of the experimental data in [6] are also shown. From a comparison of the simulated values to the experimentally extracted values for capacitances in [6] we expect the simulated capacitances to be accurate within 5 %.

From the simulations we expect a capacitive nearest neighbor coupling of around 29 fF. A comparison to the expected 1 fF coupling between second-nearest neighbor sites indicates that we are well within the tight-binding regime such that a theoretical model in which only nearest neighbor interactions are taken into account is justified.

### 3.4 Summary

To summarize the discussion about the design, we have calculated the expected values of the gap frequency  $f_g$ , the coupling  $J$  and the unit cell impedance  $Z$  from the simulated values in the tables above.

	Lower gap edge $f_g$	Coupling $J/(2\pi)$	Unit cell Impedance
Simulated	7.85 (48) GHz	239 (25) MHz	38.4(24) $\Omega$
Expected	8.27 (54) GHz	243 (32) MHz	40.2(27) $\Omega$

Table 3: Estimated resonator properties for the CRAs in Fig. 9 as obtained from values quoted in Tables 1 and 2. The error estimates result from conventional linear error propagation. The simulated value is calculated from the expected inductance together with the simulated capacitances assuming relative errors of 12% and 5% respectively. The expected values were obtained from the expected inductance and the expected capacitances extrapolated from the experimental values in [6] (see Appendix E).

## 4 Experimental Studies

### 4.1 Experimental Setup and Conditions

All measurements have been performed as dipstick measurements in a liquid helium dewar at temperatures of about 4.2 K. This is well below the critical temperature of superconducting niobium, which typically lies around 9.2 K. The scattering matrix elements  $S_{11}, S_{12}$  were measured with a four-port VNA of type Agilent N5230. Before the measurements the VNA was connected to the dipstick device and a calibration of the dipstick cables at room temperature was done without the chip at the end. The bottom end of the dipstick is shown in Fig. 10. Since the calibration was done at room temperature, the absolute values of the scattering matrix elements exceeded 1.0 when the dipstick was put into the liquid helium dewar. This necessitated a normalization of the obtained data. For all data plots in this section we carried out zeroth order normalization of the scattering parameters by dividing through the maximal absolute value of the respective trace, if this maximal value exceeded 1.0.

### 4.2 Experimental Results

We have measured the scattering parameters of eight samples of the M77 series, under nominally identical conditions. In the chosen samples, different features of the design were varied in a controlled way and one at a time, including: degree of symmetry of the unit cell, number of sites, type of turn element. We also measured two nominally identical samples to get a qualitative impression to what extent fabrication inhomogeneities affect device performance. Our observations are reported in the remainder of this section. For schematics of the measured chips we refer to the appendix.

#### 4.2.1 Symmetric vs. Non-Symmetric Unit Cell

The first experiment compares the transmission amplitudes for two resonators that differ only in the way the capacitance and inductance is distributed in the physical implementation. For one resonator the finger capacitors are distributed evenly to the left and right of the inductors (‘symmetric’) while for the other resonator the finger

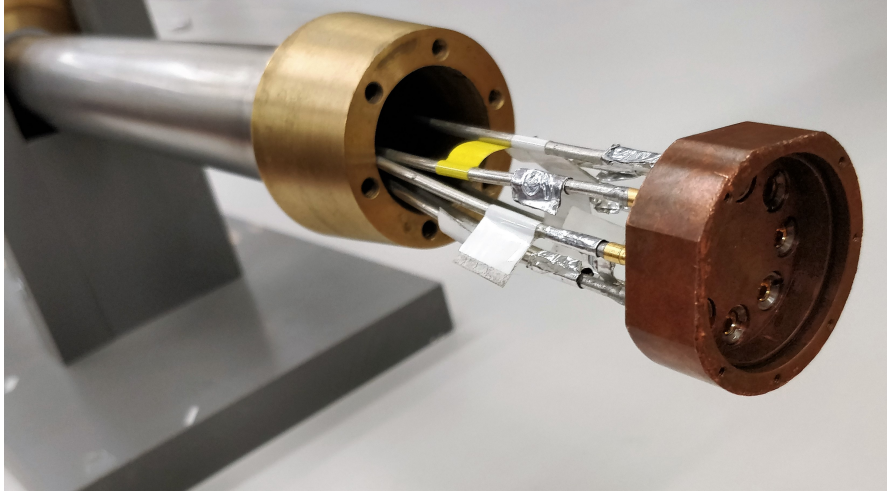


Figure 10: A picture of the bottom end of the dipstick. The chip is placed on a copper PCB (not shown) and fully enclosed in the copper shielding at the bottom end of the dipstick. This shielding is then fully submerged into liquid helium.

capacitors are completely on one side of the inductors (‘non-symmetric’). Interestingly, the resonance frequencies of these two resonators differ by 0.3 GHz [Fig. 11(b)]. We have identified three possible reasons for this shift.

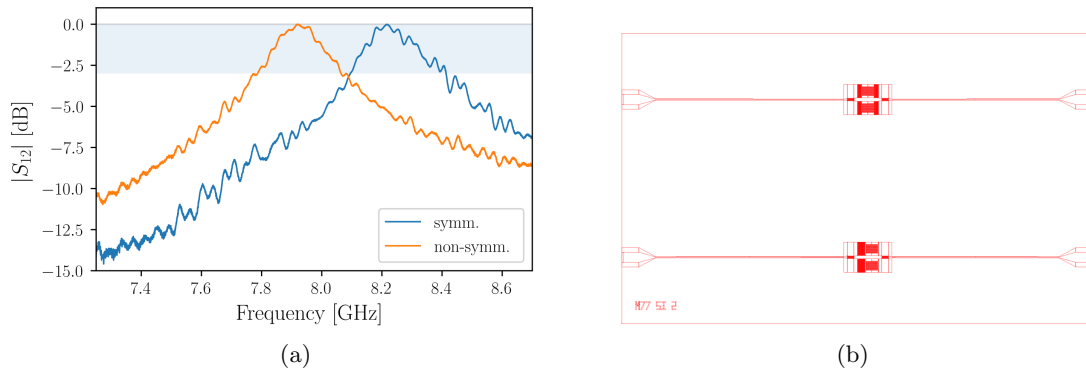


Figure 11: The schematic in panel (b) shows the chip with a symmetric resonator (top) and a non-symmetric resonator (bottom). Symmetric and non-symmetric here refers to the left-right symmetry. Both resonators have top-bottom symmetry and have the same designed total inductance and capacitance. The normalized spectra of these two resonators is shown in panel (a). The  $-3$  dB band is shaded in blue. Note that the resonance frequencies differ by 0.3 GHz.

Firstly, the dipstick measurement on this chip was done without air bridges or wire bonds on the chip, i.e. only wire bonds between the chip and the PCB were used.

Although the resulting effects are not immediately obvious, it could be that this affects one of the two resonators more than the other.

Secondly, the splitting of the capacitors leads to the development of a new symmetry axis. If there are any compensation currents in the non-symmetric design, it is likely that these are significantly reduced by the additional symmetry. Since compensation currents can affect the inductance of the resonator, this could explain the frequency shift. Assuming that the capacitance is the same for both designs we find with the relations from Section 2 that  $L_{\text{n.s.}} = (f_{\text{s.}}/f_{\text{n.s.}})^2 L_{\text{s.}} \approx 1.07 L_{\text{s.}}$ , signifying that the inductance in the non symmetric case is 7 % larger. To experimentally test this hypothesis one could do a laser scanning microscopy of the chip and check for compensation currents.

As a third point there could be other effects from splitting the finger capacitors that we have not yet considered. For example, the splitting of the finger capacitors could reduce the total capacitance due to the larger distance between the two capacitor parts and hence increase the resonance frequency. This specific effect could be assessed with a DC analysis of the two resonators<sup>8</sup>. To explain the shift in resonance frequency purely from a change in capacitance, the capacitance in the non-symmetric case would have to be about 7 % larger than in the symmetric case by the similar arguments as in the previous paragraph.

The question of what causes the resonance frequency to shift between these two resonators is interesting because it could shed light on the discrepancy between experimentally measured and theoretically calculated inductance in [6] as mentioned in Section 3.2. If the resonance frequency shift is due mostly to an inductance increase from compensation currents, then this indicates that such currents have the required order of magnitude to explain the inductance discrepancy. And since the design in [6] possess no symmetry axis, it is highly likely that such compensation currents are present. Settling this issue would pave the way for more accurate inductance estimates and thereby improve the frequency estimates for future designs.

#### 4.2.2 Scaling of the Transmission Envelope and Delay

An important feature of the theoretical model is that the envelope of the resonances above the lower gap edge  $f_g$  did not change significantly as we increase the number of sites. To check whether this feature is correctly captured in our implementation an overlay of the transmission amplitudes for linear resonator arrays with 1, 3, 5 and 10 resonators are shown in Fig. 12. For all chips in this comparison the coupling to the outside  $C_t$  was provided by a finger capacitor with 10 fingers.

We can conclude that at least the linear lumped element CRAs, that is arrays without turns, capture this feature of the theory well. Another important theoretical feature is that in the lossless case all individual resonance peaks at frequencies higher than  $f_g$  reach unit transmission at resonance. As can be seen in Fig. 12 this is also reasonably well met in our implementation, even for the ten site resonator. Note however that

---

<sup>8</sup>We have done such a study, but did not find a systematic difference. However, for this study we have not used a very small error tolerance in Maxwell and it might pay off to rerun the simulations with higher precision.

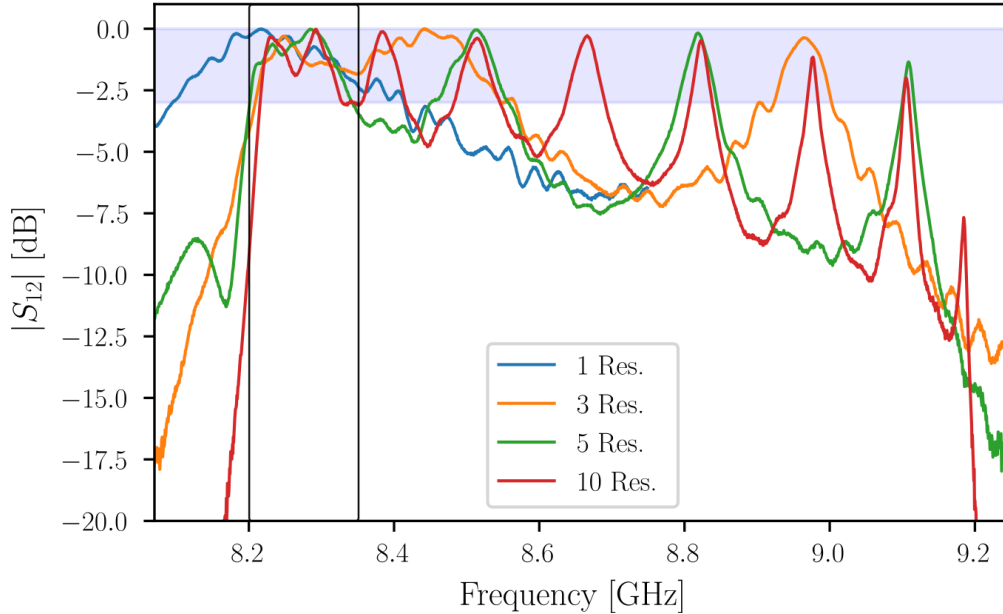


Figure 12: The transmission amplitude  $|S_{12}|$  for four CRAs with 1,3,5 and 10 sites is shown. The  $-3$  dB band, which indicates a drop in the transmitted power by a factor of 2, is shaded in blue. Note that the envelope at frequencies higher than the lower gap edge  $f_g \approx 8.22$  GHz stays the same as the number of sites is increased. This is expected from transfer matrix simulations. Note the spurious resonance at 8.1 GHz in the transmission spectrum of the 5-site resonator array (green). A closeup of the black box around the gap is shown in Fig. 13.

since the calibration was done at room temperature, the spectra were normalized to unit transmission<sup>9</sup> [Section 4.1]. This means that one cannot tell from Fig. 12 whether all cases have the same non-zero loss.

In Fig. 13 a closeup of the boxed region at the lower gap edge is plotted to see how the small developing transmission band at  $f_g$  and corresponding delay are affected by the number of sites in our implementation. This delay is calculated from the phase of the transmission parameter [Eq. (27)] and not directly measured from a pulse. Note that there is a slight variation of about 20 MHz in the lower gap frequencies  $f_g$  of the different arrays, which causes the curves to be slightly shifted with respect to each other. We attribute this to manufacturing inhomogeneities and slightly different environments for the CRAs on different chips. By looking at the 10-site resonator array, we see that we can reach about 17 ns group delay in a band of 10 MHz at almost unit transmission.

<sup>9</sup>For the spectra shown here, the maximal values of the unnormalized spectra were 1.27, 1.23, 1.23 and 1.20 for the 1,3,5 and 10 resonator cases respectively.

The simulated maximal value for this structure is 18 ns. We conclude that the simple theoretical model of a chain of LC resonators works well for the designed linear resonator arrays.

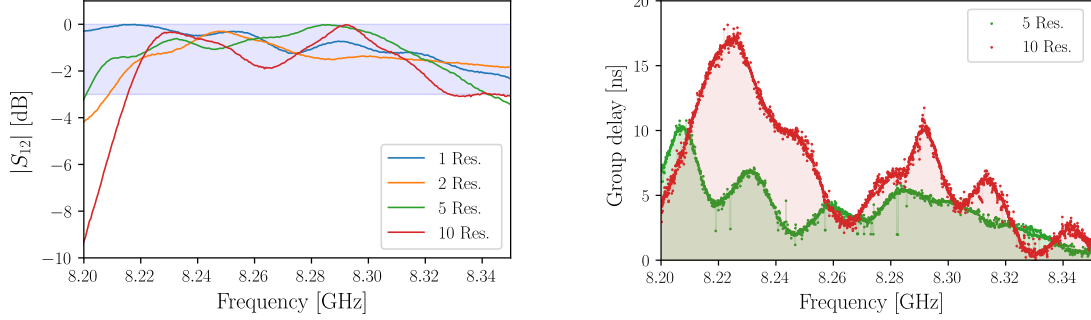


Figure 13: A closeup of the band gap region marked by the black box in Fig. 12 is shown along with the corresponding group delay for the 5 and 10 site CRAs. The  $-3$  dB band is shaded in blue.

### 4.2.3 Fabrication Inhomogeneities

For the development of a flat transmission band with large delay around the lower band gap it is imperative that the individual resonators are as similar to each other as possible. Hence, fabrication inhomogeneities can play a big role. To check whether significant fabrication issues are visible in the implementation, we have compared two nominally identical designs. Fig. 14 shows the transmission spectra of two nominally identical ten-site resonator arrays on different chips.

The two spectra are remarkably similar, but there is a slight difference of about 10 MHz in the frequency at which the gap develops. Having these gap frequencies match very well could thus prove as a challenge when several linear arrays are stacked together. We have not yet studied theoretically what happens to the developing band when we stack CRAs with slightly different gap frequencies  $f_g$  together. However, we have investigated the effect of inhomogeneities at the single resonator level and found that the relevant scale for the tolerance is characterized by  $J$ . More precisely, for the hybridization of transmission peaks into a small band at the lower band edge the spread in the resonance frequencies should stay well below the inter-site coupling rate  $J$ . To achieve this for couplings on the order of 100 MHz, the circuit parameters should vary less than 5% between individual sites. The delay at the transmission peak closest to the band gap varies between 21 ns and 17.5 ns for the blue and orange curve respectively.

### 4.2.4 TL-Turns vs. R-Turns

Our experiment also shed light on the question of whether to proceed with TL-turns or R-turns, brought up in Section 3.1.

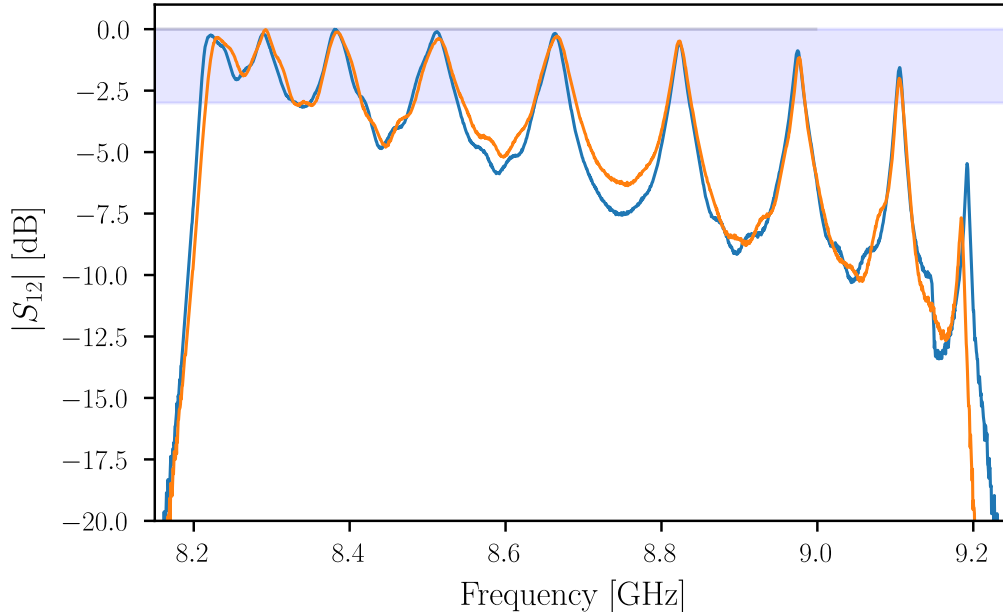


Figure 14: The transmission spectra  $|S_{12}|$  identical ten-site resonator arrays are shown.

In the tested samples with turns the 3-site coupled resonator arrays containing an R-turn exhibited poor transmission amplitudes as compared to linear 3-site CRAs [Fig. 15]. In two of four cases the R-Turn transmission amplitude spectrum is plagued by spurious modes within the region of the transmission band in the infinite site limit, which limits the peak transmission to about  $-10$  dB.

Our analysis remained inconclusive about the cause of the poor performance of these R-Turn samples, but we suspect that it might be connected to the fabrication process. As the photo lithographic process has a different precision in different directions it is possible that the orientation, i.e. the horizontal/vertical alignment, of a resonator with respect to the chip borders affects its resonance properties. For R-turn resonators the turned site at the edge has a different orientation from the sites within the linear segment. This could then lead to a mismatch between the sites in the linear segment and the turned sites at the edges, possibly causing the features we observe in the transmission amplitude spectrum.

Further evidence for the hypothesis that horizontally and vertically aligned resonators differ in their properties is provided by the spectra of the two-site TL-turn CRAs shown in Fig. 16. Two nominally identical two-site arrays on the TL-turn chip, one written horizontally and one vertically, differ in their gap frequency by almost 0.2 GHz.

On another note, it could also be that this frequency shift is due to the different angle at which the transmission line approaches the resonators and the resulting different partitions of the ground plane.

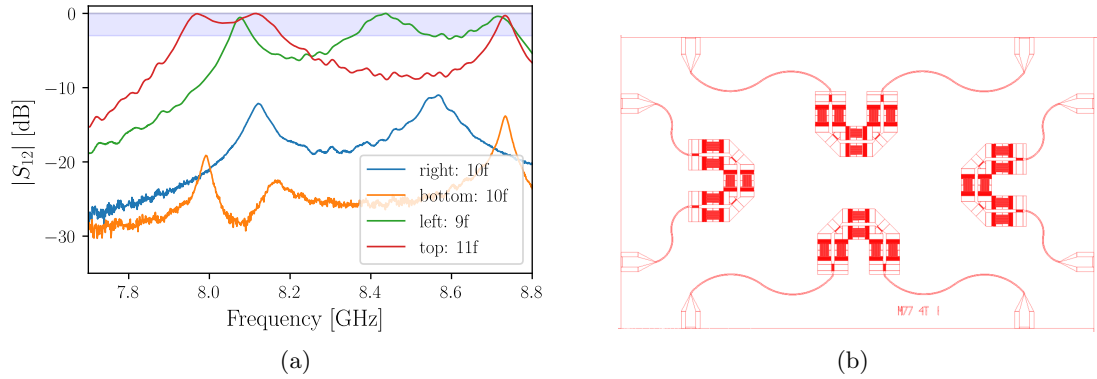


Figure 15: (a) The transmission amplitude for the R-Turn structures in the schema in (b) are shown. Note the particularly poor transmission amplitudes for the samples on the right and on the bottom of the chip. Both samples have termination capacitors with 10 fingers. Only the 'top' sample shows the expected transmission amplitude for a three-site resonator.

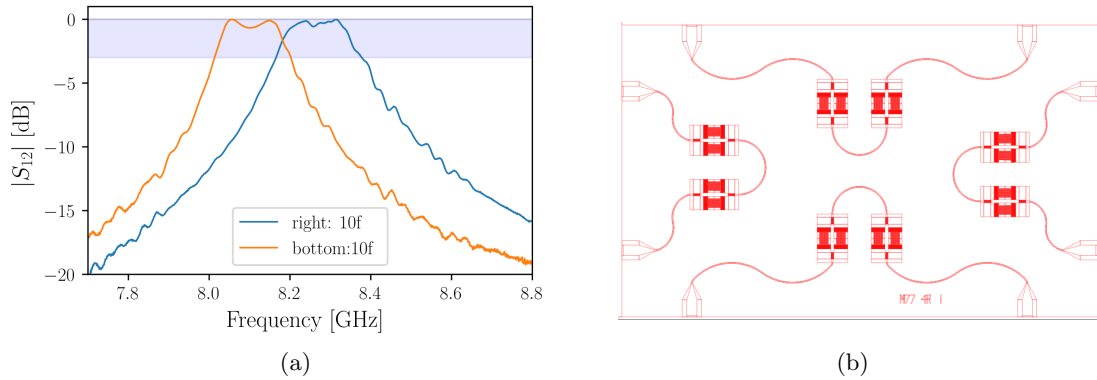


Figure 16: (a) The transmission amplitude for the for the samples at the bottom and at the right corner of the chip schema in (b) are shown. Both samples are nominally identical two-site resonators with a TL-turn. The bottom sample has vertically aligned resonators while the resonators in the sample on the right are horizontally aligned. Notice that the gap frequencies  $f_g$  of the two samples differ by 0.2 GHz. The gap frequency of the horizontally aligned resonator array is at  $f_g \approx 8.2$  GHz, which is in accordance with the resonance frequency of the other horizontally aligned samples.

#### 4.2.5 Parameter Extraction

To extract the circuit parameters from the measurements we fitted the complex S-parameters in reflection and transmission with the theoretical model from Section 2.

**Single-Resonator Measurements** According to [6] it is not possible to determine the LC parameters ( $C$ ,  $L$ ,  $C_t$ , possibly  $R$ ) purely from the resonance properties of a single resonator ( $f_0$ ,  $\kappa$ ,  $\gamma$ ). The following two reasons are given for this.

- To extract reliable parameters an accurate calibration of the entire dipstick device down to cryogenic temperatures is needed. Such a calibration must be done with calibration standards suitable for those temperatures.
- Even if the resonance frequency and the coupling and loss rates were measured perfectly this would not be enough to extract the circuit properties of a single resonator. An additional parameter, the phase shift  $\Phi$  far from resonance, would be needed for parameter extraction. However, this phase will depend strongly on the external environment, making an accurate measurement unfeasible.

We thus conclude that an extraction of the LC parameters with measurements of individual resonators does not seem possible in our case<sup>10</sup>. The extracted resonator parameters from a single resonator fit are shown in the table below.

$\omega_0/2\pi$	$Q_l$	$\kappa/2\pi$
8.207 GHz	42.1	195 MHz

Table 4: Resonator parameters as obtained from a single resonator fit. A lossless resonator was assumed, attributing the quality factor fully to the out coupling  $\kappa$ . The out coupling was provided by a 10-finger finger capacitor ( $C_t$ ).

**CRA Measurements** Since we measured not only single resonators but also resonator arrays with many nominally identical resonators, there is hope that it might be possible to extract the parameters from a fit of the multiple peak spectrum of these arrays. We have tried this, but it turned out that the residual function has numerous local minima, which makes it possible to find many combinations of circuit parameters that fit the same S-parameters.

This makes algorithmic fitting difficult since the fit will typically converge to the local minimum closest to the provided starting values. The problem can be circumvented by fixing one of the LC parameters and fitting for the others. For the fits presented here we have fixed the value of the shunt capacitance  $C$  since we have simulation estimates as well as experimental estimates from a similar design (see Table 2).

An additional complication for the fitting is that the experimental values for  $S_{11}$  and  $S_{12}$  do not have the correct magnitude (their modulus can exceed 1 [Section 4.1]) due to the calibration of the dipstick cables at finite temperatures. This makes it necessary to normalize them, which leads to a loss of information.

<sup>10</sup>To be more precise, it is possible to extract the circuit parameters of a single resonator purely from measurements if one measures two identical resonators in a weak ( $C_t \ll C$ ) and strong coupling limit ( $C_t \sim C$ ) as done in [6].

Chip	$f_g$ [GHz]	$C$ [fF]	$L$ [nH]	$C_\kappa$ [fF]	$C_t$ [fF]	n
SI (sym.)	8.207	400*	0.752	-	50 (10f)	1
S3 (sym.)	8.244	400*	0.732	26.2	54.8 (10f)	3
F120 (10f)	8.220	400*	0.739	25.7	53.5 (10f)	5
NT (10f)	8.203	400*	0.744	26.3	53 (10f)	10
NT (9f)	8.213	400*	0.750	25.9	46.3 (9f)	10
TE (10f)	8.205	400*	0.735	25.7	56.0 (10f)	10

Table 5: The parameters  $f_g, C, L, C_\kappa$  and  $C_t$  as estimated from the fitting procedure explained in the main text are shown. Values with a \* have been held fixed during optimization. Since the parameter space of the fit function has a one dimensional degeneracy it is not possible to obtain values for the circuit parameters without fixing one of them. Using the expected value of 400 fF for the capacitance [Table 2] we expect the other parameters to be accurate to within 10%. From the fitted values it is clear that the 10f version achieves the best coupling.

Also, the phase of the transmission and reflection coefficients are not easy to extract, since the calibration does not include the chip at the end of the dipstick. To go around this problem we had to introduce two additional fit parameters, a phase offset for the transmission phase and the length of the circuit on the chip.

**Fitting procedure** Prior to any fitting the maximal magnitudes of  $S_{11}$  and  $S_{12}$  were normalized to 1. We then fixed the value of  $C = 400$  fF and fitted the S-parameters for the gap frequency  $f_g$ , coupling capacitance  $C_\kappa$ , termination capacitance  $C_t$  and circuit length  $l$  as well as two constant phase shifts  $\phi_t$  and  $\phi_r$  with the in a least squares fit. The fit function was obtained from a transfer matrix calculation as explained in Section 2. The results of the fits are summarized in Tab. 5. The circuit length  $l$  was estimated to be about 7.9 mm in all cases, which agrees well with the length of the chip plus a bit of PCB. As an example we show the plotted spectrum of the S3, F120 and NT chip together with the fit in Figs. 17, 18 and 19.

S3 1 - Three Symmetric Resonators

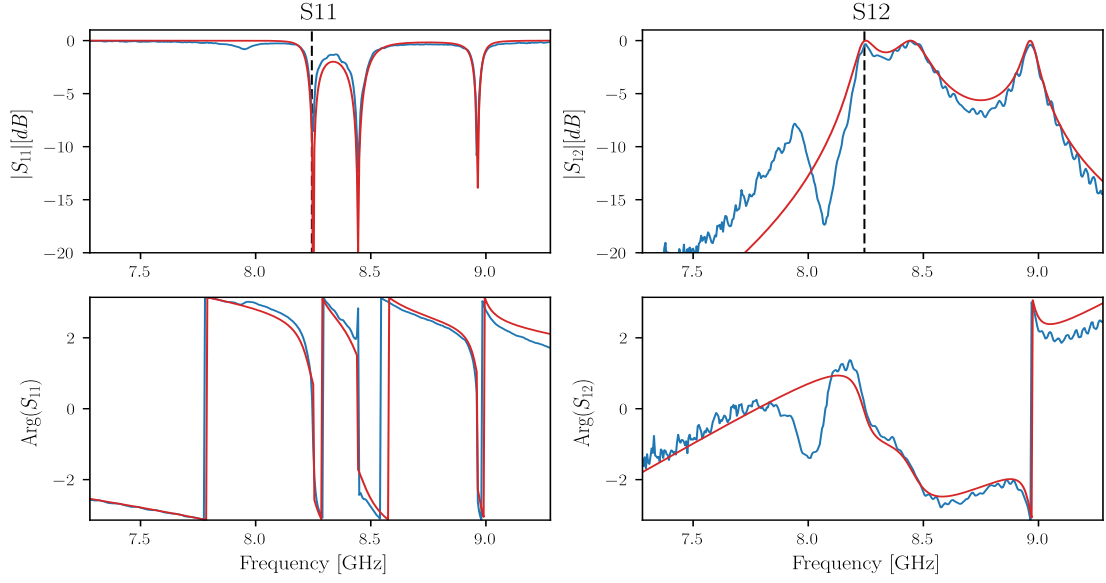


Figure 17: Fits for a linear array of three symmetric resonators on the S3 chip. The data is shown in blue, the fit in red.

F120 - Five symmetric Resonators

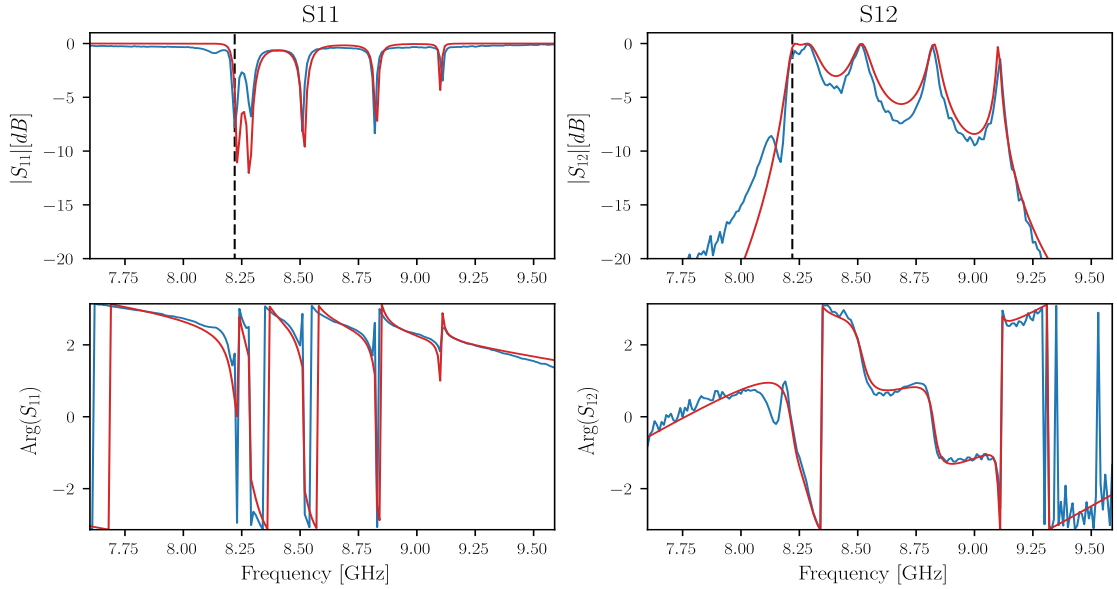


Figure 18: Fits for a linear array of five symmetric resonators on the F120 chip. The data is shown in blue, the fit in red. The data is shown in blue, the fit in red.

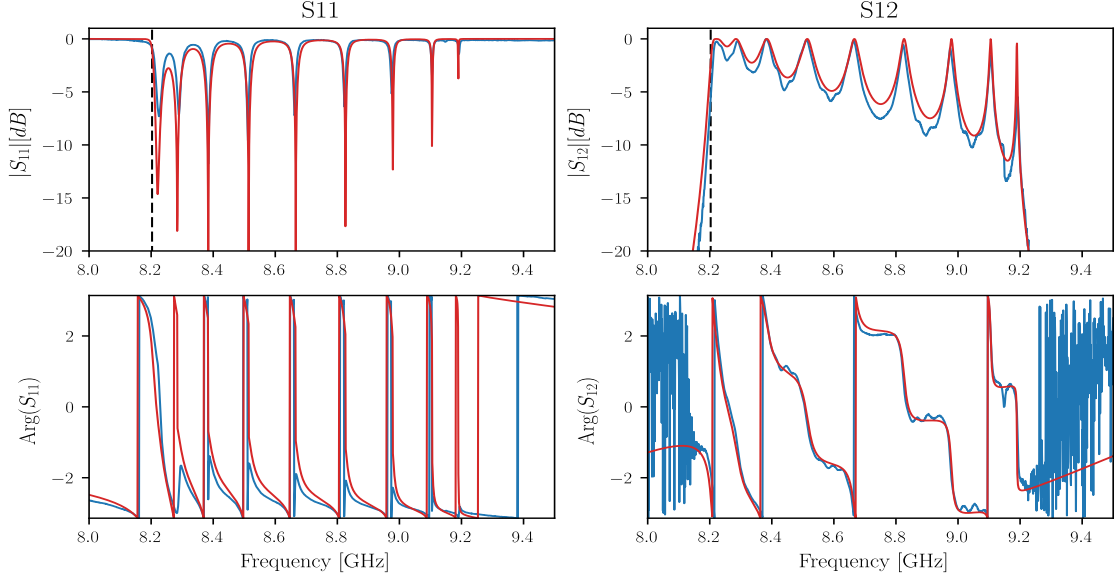


Figure 19: Fits for a linear array of ten symmetric resonators on the NT chip. The data is shown in blue, the fit in red.

## 5 Conclusion and Outlook

To conclude this discussion we briefly recap the main learnings as well as some of the remaining challenges of this first round of CRA experiments. We will also present a few ideas on how to improve on this first experiment. Let us start with the main learnings.

- With the M77 chip series we can reach a delay of about 17 ns at almost unit transmission with an array of 10 sites. If we sacrifice some of the signal, we can even get 35 ns at a transmission amplitude of about 0.7.
- At least for linear resonator arrays the theoretical model of a chain of LC resonators fits the experimental data very well. This is remarkable, since the LC chain model has just 5 parameters.
- The generation of a 10 MHz wide transmission band at the frequency of the developing gap edge is possible with linear array., However, keeping the transmission flat and above  $-3$  dB in a range of 10 MHz proves difficult once we incorporate turns.
- To achieve the matching condition  $C_t = 2C_c$  within 5% it is sufficient to simply have twice the amount of finger on the  $C_t$  finger capacitor. For a larger precision a more accurate estimate of the circuit parameters is needed.

- It is not possible to extract the circuit parameters from our simple measurements, unless we fix one of the parameters. This is due to the high degeneracy of the parameter space, which makes the fit converge to an arbitrary local minimum close to the starting values.
- For the development of a transmission band it is crucial to have the sites as identical as possible. If one resonator is slightly damaged the chip is useless.
- Turns with resonators are difficult to implement physically as the fabrication process seems to distinguish between horizontally and vertically aligned resonators.

From this discussion we clearly see three main challenges to improving upon the present design.

The first challenge is to build a proper turn at the end of linear resonator arrays that allows to scale the number of sites while keeping their properties as identical as possible. In this study we have tried two approaches. One approach was a resonator turn. This approach failed presumably because of a difference in the fabrication procedure for horizontally and vertically aligned resonators. The other approach was a transmission line turn. This option proved more promising, especially as it was not optimized in the current design.

A second challenge is the proper estimation of LC circuit parameters. With our current measurements we could extract the circuit parameters only after fixing one parameter. Ignorance of the actual circuit parameters hinders the further optimization of the matching condition  $C_t = 2C_c$  as well as a more precise estimate of the resonance frequency. Having good estimates of the inductances and capacitances of the physical design can furthermore hint at possible compensation currents or other parasitic contributions. An understanding of such contributions can improve the design process.

Finally, a third challenge is the fabrication homogeneity. It is important to have very similar unit cells when we try to scale the number of sites in the resonator array. The reason is that for the hybridization of transmission peaks into a small band at the lower band edge the spread in the resonance frequencies should stay well below the inter-site coupling rate  $J$ . To achieve this for couplings on the order of 100 MHz, the circuit parameters should vary less than 5% between individual sites.

## Outlook

The following is a non-exhaustive list of possibilities to improve on this first experiment and learn more about the resonator arrays.

**Studying an RLC model** In the theoretical lumped-element studies we have so far always assumed a lossless circuit. Even though superconductors have virtually no dissipation, our resonators should be simulated as RLC circuit as other effects, such as dielectric losses, may well play a role. This addition does not notably complicate simulation and could provide valuable insights into how the band is affected by nonzero loss. It might also improve the fitting.

**Settling the Symmetric vs. Non-symmetric question** To settle the question of why the nominally identical, symmetric and the non-symmetric resonators differ considerably in their frequency a high-frequency electromagnetic simulation could be done to search for inductive contributions from compensation currents. A high precision DC simulation can be used to check whether the capacitances are notably affected by the symmetric and non-symmetric geometries.

**Coplanar Waveguide Resonator Turns** The most promising approach to scale the present design is to improve the TL-turn arrays. In principle there are two ways in which the design can be optimized. We can either try to make the TL as short as possible or to match it to the wavelength and build a  $\lambda/2$  coplanar waveguide resonator. The latter approach seems particularly promising, since in theoretical simulations it reproduces the transmission spectrum that would arise if the array had no TL-turn at all. The challenge here is to match the coplanar waveguide resonator to the other resonators in the linear array. For more information on coplanar waveguide resonators we refer to [4].

**Low Temperature Calibration** To improve our parameter estimates it might pay off to investigate how we can do a low temperature calibration. Such a calibration would remove the need for an additional renormalization of the transmission amplitude and the resulting loss of information. For a better parameter estimate we could alternatively also measure identical symmetric resonators in the weak and low coupling limit, as done in [6].

**High-Frequency Electromagnetic Simulation** A high frequency electromagnetic simulation of a full chip can provide insight into the field distribution and allow to identify parasitic effects such as compensation currents, the capacitance of the inductor or the inductance of the capacitor.

**Simulation with slightly randomized Parameters** To obtain a more quantitative idea of how much fabrication inhomogeneity is tolerable, one could study a simulation of the LC chains with adding a controlled amount of disorder.

## Acknowledgements

I would like to thank Prof. Andreas Wallraff for giving me the opportunity to conduct my semester thesis in the Quantum Device Lab. A special thank you goes to my supervisors Jean-Claude Besse and Simone Gasparinetti. They offered me a a very rich experience which included theoretical calculations, simulations, coding and chip design as well as hands on experience in the lab. Moreover, they helped me with their advice when I got stuck. The many fruitful discussion have given me exciting insights into the physics of circuit quantum electrodynamics. I would also like to thank Michele Collodo, who supported me with his knowledge of lumped element resonators.

## A Motivation of the Bloch Condition

To give a physical intuition about how the Bloch condition arises due to discrete translational symmetry, we examine explicitly the example of a 1D ring of resonators. For a full derivation of the general Bloch Theorem we refer to literature, e.g. [5].

Let us look at a circular array with  $N$  unit cells, each of length  $a$ . Due to the discrete translational symmetry, no point  $z$  on the ring is different from the point  $z + a$ . We thus expect that the voltage at  $z$  differs at most by a factor  $C$  from the voltage at  $z + a$

$$V(z + a) = CV(z). \quad (28)$$

If we proceed in this manner for a full round trip around the ring, we obtain

$$V(z + Na) = C^N V(z) = V(z). \quad (29)$$

Thus,  $C$  must be a root of one, i.e.  $C = \exp(2\pi in/N)$  with  $n$  being an integer. This means that

$$V(z + a) = e^{i\frac{2\pi n}{Na}a} V(z) = e^{ik_n a} V(z), \quad (30)$$

where we defined the reciprocal lattice vector  $k_n = 2\pi n/Na$ . This is precisely the Bloch condition in the case of periodic boundary conditions in one dimension.

## B Transformation: Design and Resonator Parameters

This is a summary of the relations between the design parameters ( $C, L, C_\kappa, C_t, N$ ) and the physical resonator parameters ( $\omega_0, Z, J, \delta, N$ ). The indicated approximations hold for  $C_\kappa, C_t \ll C$ .

$$\omega_0 = \frac{1}{\sqrt{LC_\Sigma}} \approx \frac{1}{\sqrt{LC}} - 2J \quad (31)$$

$$Z = \sqrt{\frac{L}{C_\Sigma}} \quad (32)$$

$$J = \frac{1}{2} \frac{C_\kappa}{C_\Sigma} \omega_0 \quad (33)$$

$$\delta = \omega_0 - \frac{1}{\sqrt{L(C_\Sigma - C_\kappa + C_t)}} \approx \frac{1}{2} \frac{C_t - C_\kappa}{C_\Sigma} \omega_0 = J_t - J, \quad (34)$$

with  $J_t = \frac{1}{2}(C_t/C_\Sigma)\omega_0$ .

## C Definition of the group delay

Let  $S_{12}(\omega) = |S_{12}|e^{i\arg(S_{12})}$  be the frequency dependent transmission amplitude for a circuit element of interest. For a given input pulse  $f_{in}(t)$  we can write the pulse after

propagation through the element as

$$f_{out}(t) = \frac{1}{\sqrt{2\pi}} \int_{-\infty}^{\infty} S_{12}(\omega) \hat{f}_{in}(\omega) e^{i\omega t} d\omega, \quad (35)$$

where  $\hat{f}_{in}(\omega)$  is the Fourier transform of  $f_{in}(t)$ . If  $\hat{f}_{in}(\omega)$  is a narrow wave packet centered around the carrier frequency  $\omega_0$  it is appropriate to approximate the transmission amplitude around this carrier frequency. Assuming further that the phase of  $S_{12}$  varies much faster than its amplitude, we can Taylor expand the transmission amplitude around the carrier frequency  $\omega_0$ ,

$$S_{12}(\omega) \approx |S_{12}(\omega_0)| \exp\left(i \arg(S_{12}(\omega_0)) + i \left. \frac{\partial \arg(S_{12})}{\partial \omega} \right|_{\omega_0} (\omega - \omega_0)\right) \quad (36)$$

Inserting this expansion in Eq. (35), we find

$$f_{out}(t) = f_{in}(t - \tau_g) |S_{12}(\omega_0)| e^{-i\omega_0(\tau_p - \tau_g)}, \quad (37)$$

with the phase delay  $\tau_p(\omega_0) := -\frac{\arg(S_{12})}{\omega_0}$  and the group delay  $\tau_g(\omega_0) := -\left. \frac{\partial \arg(S_{12})}{\partial \omega} \right|_{\omega_0}$ .

The group delay  $\tau_g$  thus characterizes the propagation of the temporal envelope of a pulse through a circuit element. From Eq. 37 it can be seen that for a narrow pulse (or if the phase of the transmission amplitude is linear in the frequency)  $\tau_g$  gives the temporal delay of that pulse after propagating through the circuit element.

## D Inductance contribution from the island

We model the island as a piece of coplanar waveguide [4]. For a CPW the geometric inductance per unit length is given by

$$L_l = \frac{\mu_0}{4} \frac{K(k'_0)}{K(k_0)}, \quad (38)$$

where  $K$  denotes the complete elliptic integral of the first kind with arguments

$$k_0 = \frac{w}{w + 2s} \quad (39)$$

$$k'_0 = \sqrt{1 - k_0^2}. \quad (40)$$

Here  $w$  and  $s$  stand for the width of the center conductor and the gap respectively. Using values of  $w = 50 \mu\text{m}$  and  $s = 200 \mu\text{m}$  gives an inductance of  $L_l = 0.76 \text{ nH/mm}$ .

## E Parameter Estimation charts

To facilitate the future design of CRAs we have compiled capacitance and inductance estimation charts for the meandering inductors and finger capacitors presented in Section 3.

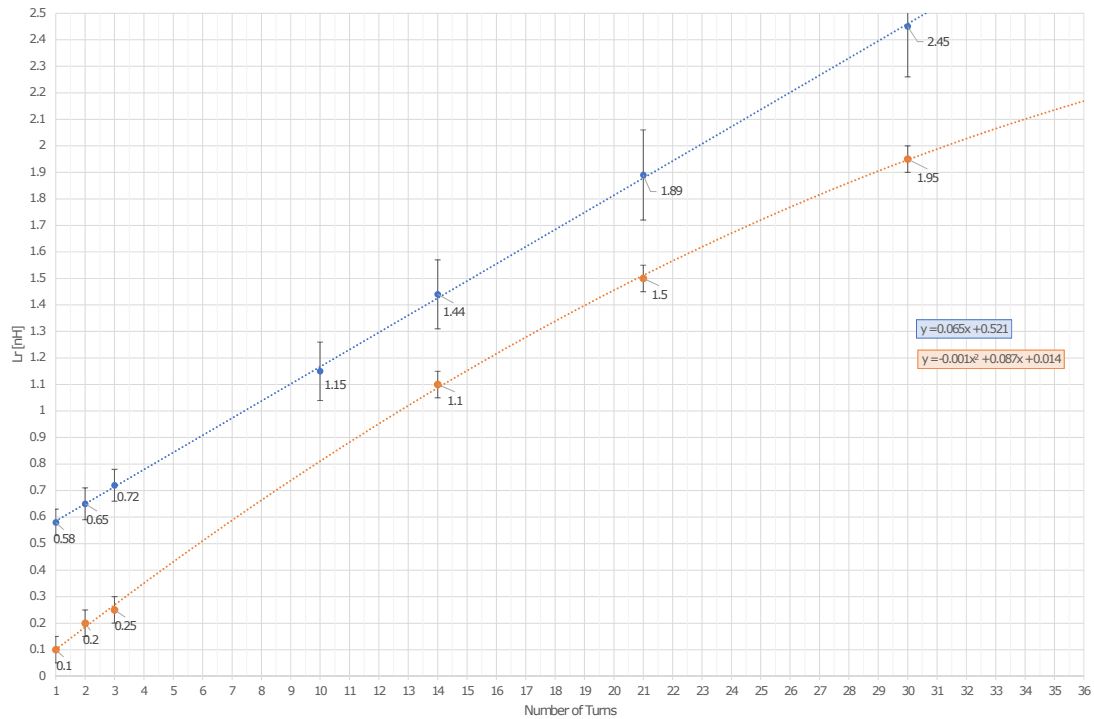


Figure 20: Inductance estimates versus number of turns for the inductor geometry specified in Table 1. The blue curve corresponds to the experimentally obtained values in [6]. The orange curve is a theoretical estimate with the methods from [7] and [6].

The data for these charts is from (i) our Maxwell simulations, (ii) our experimental data and (iii) data from [6]. Error estimates for the different sources of data come from the (i) error estimates from the simulation and (iii) values quoted in [6]. A polynomial fit is also shown as a guide to the eye and to provide a heuristic. All charts assume the geometrical parameters presented in Table 1 and Table 2.

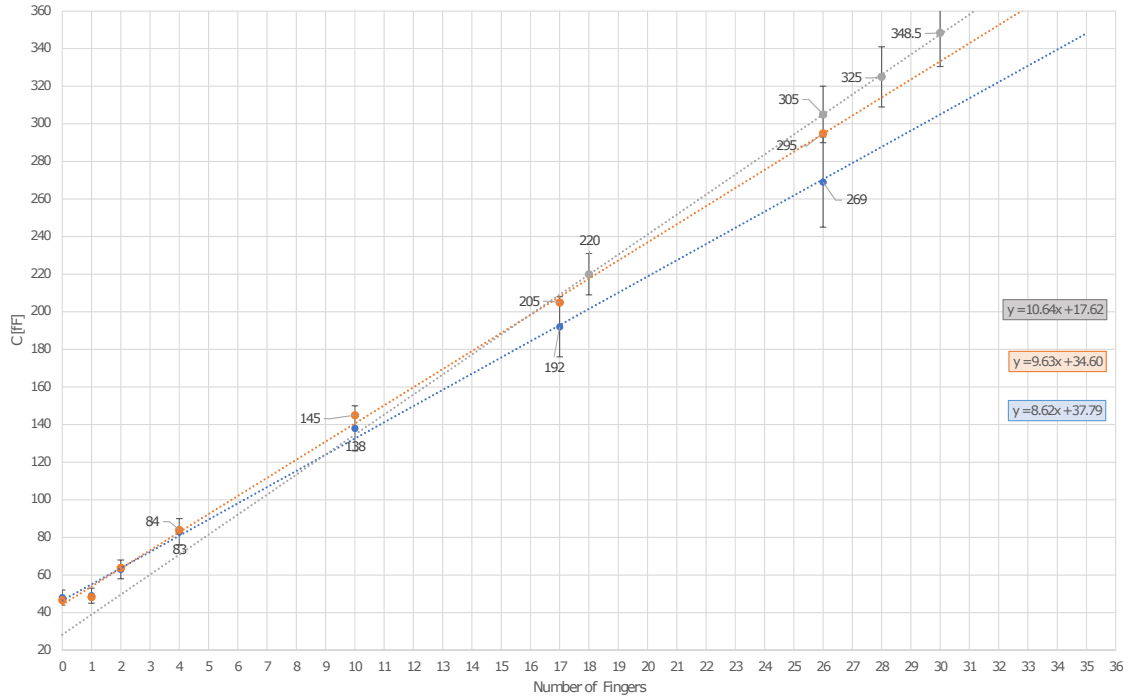


Figure 21: Capacitance estimate versus the number of fingers on a finger capacitor with geometrical parameters as for the shunt capacitors ( $C$ ) in Table 2. The gray data set is from the Maxwell simulations that we conducted for the symmetric resonator design with the inductor cut in a DC simulation. The orange points are the simulated values from [6]. The blue data points are experimental values from [6].

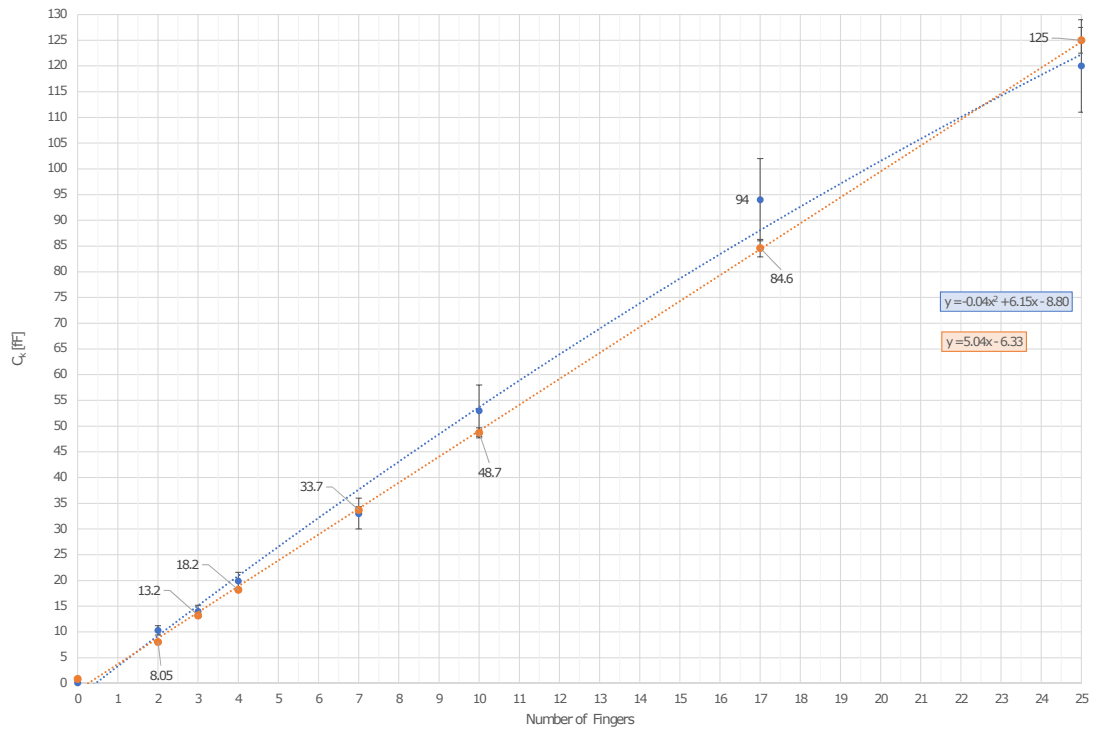


Figure 22: Capacitance estimate versus the number of fingers on a finger capacitor with geometrical parameters as for the coupling capacitors ( $C_t$ ) in Table 2. Blue data points are from our Maxwell simulations. Orange data points are from Maxwell simulations in [6].

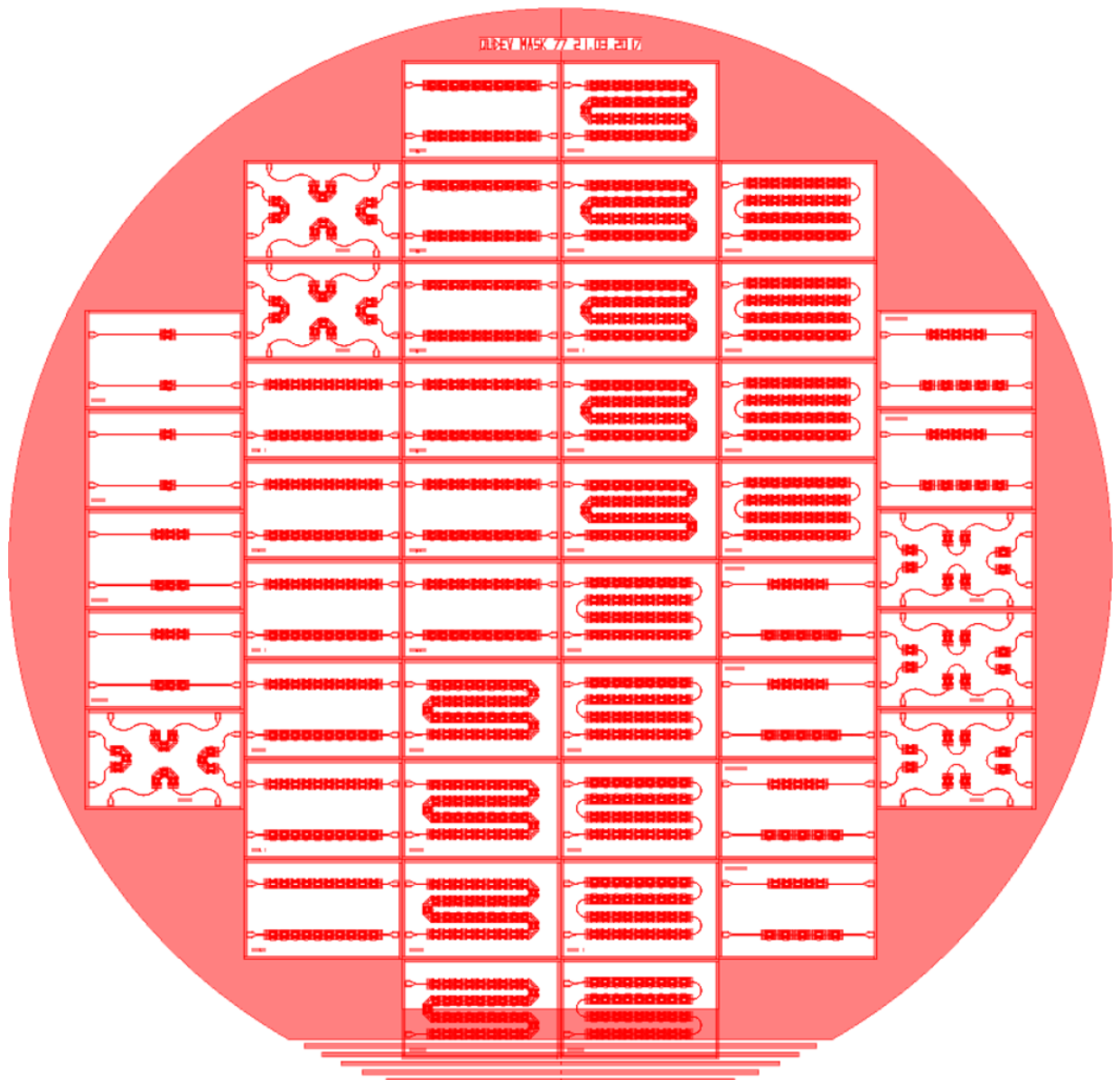


Figure 23: 2" Wafer for the M77 chip series.

## References

- [1] M. Pechal, J.-C. Besse, M. Mondal, M. Opplinger, S. Gasparinetti, and A. Wallraff. Superconducting switch for fast on-chip routing of quantum microwave fields. *Phys. Rev. Applied*, 2016.
- [2] G. Calajó, F. Ciccarello, D. Chang, and P. Rabl. Atom-field dressed states in slow-light waveguide qed. *Phys. Rev. A*, 93:033833, Mar 2016.
- [3] D. M. Pozar. *Microwave engineering*. Wiley & Sons, Hoboken, 2012.
- [4] M. Göppl, A. Fragner, M. Baur, R. Bianchetti, S. Filipp, J. M. Fink, P. J. Leek, G. Puebla, L. Steffen, and A. Wallraff. Coplanar waveguide resonators for circuit quantum electrodynamics. *J. Appl. Phys.*, 104(6):113904, Dec 2008.
- [5] F. Bassani and P. G. Pastori. *Optical Transitions in Solids*. Pergamon press, 1975.
- [6] A. R. Abadal. Josephson parametric amplifiers with lumped-element coupled resonators. Master thesis, ETH Zurich, April 2015.
- [7] L. Zivanov M. Damjanovic, G. Stojanovic. Compact form of expressions for inductance calculation of meander inductors. *Serbian Journal of Electrical Engineering*, 2004.